Detector Response Restoration in Image Reconstruction of High Resolution Positron Emission Tomography

Zhengrong Liang

Abstract—**A mathematical method was studied to model the detector response of high spatial-resolution positron emission tomography systems consisting of close-packed small crystals, and to restore the resolution deteriorated due to crystal penetration and/or nonuniform sampling across the field-of-view (FOV). The simulated detector system had 600 bismuth germanate crystals of 3.14 mm width and 30 mm length packed on a single ring of 60 cm diameter. The space between crystals was filled up with lead (i.e., septa). Each crystal was in coincidence with 200 opposite crystals so that the FOV had a radius of 30 cm. The detector response was modeled based on the attenuating properties of the crystals and the septa, as well as the geometry of the detector system. The modeled detector-response function was used to restore the projections from the sinogram of the ring-detector system. The restored projections had a uniform sampling of 1.57 mm across the FOV. The crystal penetration and/or the nonuniform sampling were compensated in the projections. A penalized maximum-likelihood algorithm was employed to accomplish the restoration. The restored projections were then filtered and backprojected to reconstruct the image. A chest phantom with a few small circular "cold" objects (≈4 mm diameter) located at the center and near the periphery of FOV was computer generated and used to test the restoration. The reconstructed images from the restored projections demonstrated resolution improvement off the FOV center, while preserving the resolution near the center.**

I. Introduction

HIGH SPATIAL-RESOLUTION positron emission tomography (PET) has been a research topic for many years [1]–[11]. It requires theoretically continuous sampling across the field-of-view (FOV) to reach the physical limit of 2 to 3 mm resolution [6]–[11]. Further improvement can be achieved by modeling the blurring effects of the positron range (from decay location to annihilation point) and the nonparallel flight of pair photons (due to nonzero positron momentum), and then compensating for the distance-dependent blurring from the center of each coincident detector pair [12].

In practice, two approaches have been taken to provide a continuous or pseudo-continuous sampling: (1) using continuous or pseudo-continuous crystals backed up with photomultiplier tubes (PMTs), in which each sampling point is determined by the weight of a few PMT's output [6]–[8]; and (2) using close-packed small crystals, in which each sampling point is localized approximately within the associated small crystal [9]–[11]. Both of the approaches have difficulty in localizing accurately the depth of the interaction site of a primary photon within the crystal. The uncertainty in localizing the interaction sites decreases the spatial resolution, especially, the resolution off the center of FOV as shown in Fig. 1 [13]–[15].

Although a similar technique can be applied to improve the resolution of the first approach by modeling the distribution of interaction sites within the continuous crystals (see the left of Fig. 1), this paper takes the second approach as an example and describes a technique which can be used to improve the spatial resolution. The technique restores the off-center resolution deteriorated due to the associated crystal penetration and/or the nonuniform sampling effects (see the right of Fig. 1), while preserving the central resolution.

Previously, two methods have been reported to compensate for the crystal penetration: (1) the hardware approach of using a position-sensitive photodiode/bismuth germanate (BGO) detector combination to localize approximately the depth of interaction within each small crystal [14]; and (2) the mathematical method of deconvolving the sinogram of the ring detector with a Monte Carlo simulated crystal-penetration kernel [15]. It is noted that many other hardware approaches have been proposed to address the crystal-penetration problem for different high resolution PET systems, for example, those as described in [9], [13], [16]–[18]. Although the hardware approach can mitigate the crystal-penetration effect, the accuracy of measurements, the complexity of detector-system design, and the cost require further investigation. The mathematical method has the potential to model the photon-interaction distribution within each crystal, and so to improve the off-center resolution without much sacrifice, except for slight increase of computation time. However, the previously reported mathematical approach achieved the gain in the off-center resolution at the expense of noisier reconstructions [15].

This paper describes a mathematical method which models the distribution of the primary-photon interactions within each crystal of the close-packed detector system (see the right of Fig. 1). The method restores the off-center resolution with a spatially-variant distribution kernel, while suppressing the noise propagation in the restoration. The distance-dependent blurring due to the positron range and the nonparallel flight of pair photons is neglected.

Manuscript received September 23, 1992; revised November 30, 1993. This work was supported by Grant #HL 44194, awarded by the National Heart, Lung, and Blood Institute. The associate editor responsible for coordinating the review of this paper and recommending its publication was C. J. Thompson.

Z. Liang is with the Department of Radiology, State University of New York, Stony Brook, NY 11794 USA.

IEEE Log 9401075.

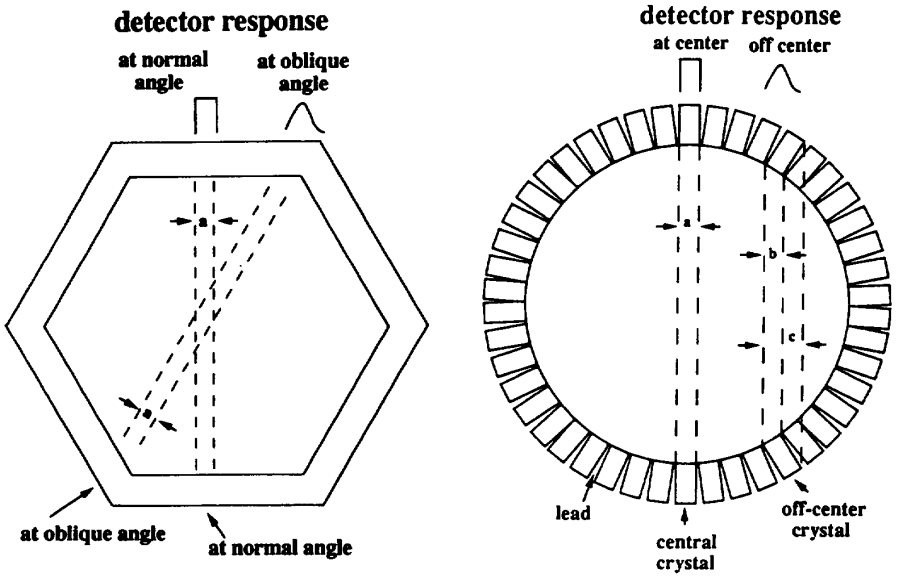

Fig. 1. Spatial resolution is degraded, in hexagonal systems consisting of continuous crystals (left), throughout the FOV due to uncertainty regarding the depth of interacting sites in the crystal. In circular systems of close-packed small crystals (right), spatial resolution is degraded as a function of radial position due to penetration of radiation into adjacent crystals. Due to the crystal penetration, detector response of each crystal varies from a nearly rectangular form at the FOV center to broadened asymmetric functions at the off-center positions. The width of the response function increases from a at the center to c off the center. If the crystals are assumed to have very high stopping power, the size of the crystal surface decreases from a at the center to b off the center. The latter variation is called nonuniform sampling effect.

II. Methods

To describe the restoration method, we make use of the specifications of a detector system somewhat similar to the Donner PET scanner [19], [20]. A simplified diagram is shown on the right of Fig. 1. The detector system has 600 BGO crystals of 3.14 mm width and 30 mm length packed on a single ring of 60 cm diameter. The space between crystals is filled up with lead (i.e., septa). Each crystal is in coincidence with 200 opposite crystals so that the FOV has a diameter of 30 cm. The sinogram of the detector system consists, for stationary scan, of 600 projections uniformly spaced over 180 degrees. Each projection has 100 or 101 samples (or detector pairs) nonuniformly distributed across the FOV. The size of the crystal surface projected to the FOV varies from $a = 3.14$ mm at the FOV center to $b = 2.72$ mm at the periphery, while that of the whole crystal from $a = 3.14$ mm to $c = 17.72$ mm. The detector response is modeled, as a probability distribution of the primary-photon interactions within each crystal, based on the attenuating properties of the BGO crystals and the lead septa, as well as the geometry of the detector system [21], [22]. The coincident response of pair-photon detection is neglected in this model. Since the coincident response depends on the distance from the center of the detector pair, it can be incorporated into the distance-dependent blurring of positron range and nonparallel flight of pair photons and be considered during reconstruction (as will be discussed later). In the followings, we will focus on the restoration of detector response (which is associated with the primary-photon interactions within close-packed small crystals) prior reconstructing images.

For the central crystal, the probability distribution of photon interactions is expressed as:

$$p_{\mathrm{ctr}}(t) = 1 - \exp(-\mu_b H) \tag{1}$$

where t is the radial coordinate, μ_b the attenuation coefficient of BGO crystal, and H the length of the crystals. For the off-center crystals, the probability distribution becomes:

$$p_{\mathrm{off}}(t) = \{1 - \exp[-\mu_b\, y(t)]\} \exp[-\mu_b\, h(t) - \mu_l\, l(t)] \tag{2}$$

where $h(t)$ is the sum of intersecting lengths of a primary-photon path (at radial position t) within crystals in front of the concerned crystal and detected by the next encountered crystal, $l(t)$ is the sum of intersecting lengths of the primary-photon path within the lead septa in the front of the concerned crystal, $y(t)$ is the intersecting length of the primary-photon path with the concerned crystal, and μ_l is the attenuation coefficient of lead.

Fig. 2 shows the probability distributions of five crystals which are located at the FOV center and off the center by 3.14, 6.25, 9.42 and 12.56 cm, respectively. The five probability-distribution curves are concatenated with one unit separation in the figure. So the horizontal index reflects the relative width of the probability distribution across the FOV. The probability distribution for the central crystal has a rectangular form with height of 0.93 over 3.14 mm width or 3 unit width (see the left peak in Fig. 2). The probability distribution for the off-center crystals varies as a broadened asymmetric shape, depending on the radial position. For example, the probability distribution for the crystal at radial position 12.56 cm off the center has the peak height of 0.39 over 17.72 mm width or 10

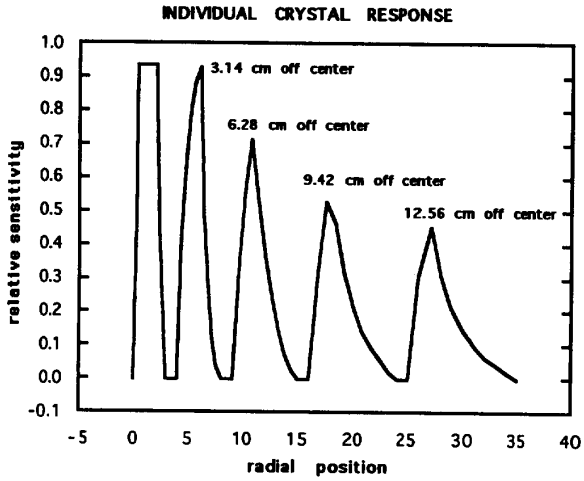

Fig. 2. The response for each individual crystal at the FOV center (a rectangular form) and off the center by 3.14, 6.28, 9.42 and 12.56 cm (broadened asymmetric shapes). The response peak is lower for the off-center crystal, but the distribution has a larger range due to the larger size of the projection of off-center crystal length on the FOV. The width of each peak represents the relative crystal size projected across the FOV.

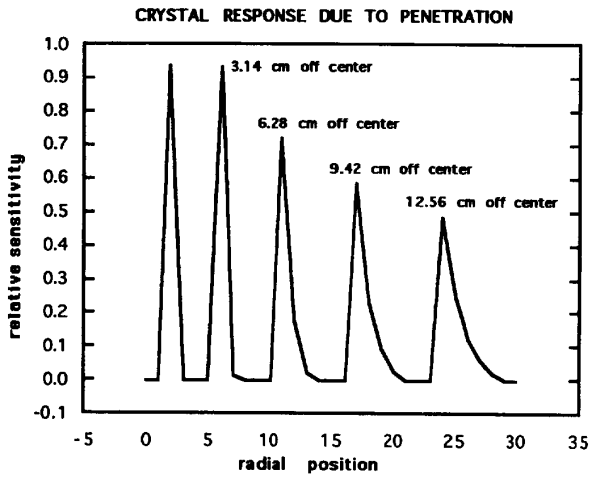

Fig. 3. The response for a few crystals associated with a primary-photon history. Since there is no crystal penetration for the central crystal, the detector response is a single peak. For the off-center crystals, a primary photon may be detected by the first encountered crystal with the probability valued at the left of the peak, or penetrates one or more crystals and septa, and then is detected by the last encountered crystal with the probability valued at the right of the peak. The width of each peak represents the relative number of crystals penetrated.

unit width (see the right peak in Fig. 2). In order to minimize the sharp change near the four corners of the rectangular crystal in the computed results, the probability distributions are usually smoothed slightly by a filter (say a Gaussian filter). The detector-response function of Fig. 2 associated with each individual crystal is essentially the same as that of Monte Carlo simulated as presented in [21]–[24].

Theoretically, the simulated spatially-variant detector response of Fig. 2 can be used to compensate for the crystal penetration. However, because the response function is continuous within each crystal, the associated computation for the compensation is very intensive. Instead, another detector response function is used, which is generated based on the individual crystal response of Fig. 2, as shown by Fig. 3. The five responses at different radial positions are plotted in Fig. 3 in a similar manner as in Fig. 2, i.e., they are concatenated with a separation of two units. The width of a response reflects the relative number of crystals being penetrated at the corresponding radial position. This modified response function represents the probability distribution of a primary photon being detected by all encountered crystals. For example, the response at the radial position through the central crystal (the left peak in the figure) is, since there is no crystal penetration, a peak with a value of 0.93 over a unit width. The response at the radial position through the crystal at 3.14 cm off the center (the second peak from left in the figure) is similar to the response through the central crystal, except for that it has a small tail at the right hand side (RHS) of the peak. The small tail reflects a small fraction of primary photons passed through the first encountered crystal and detected by the next encountered crystal. At the radial positions through other off-center crystals, since the primary photons have nonzero probabilities to penetrate more crystals and septa, the responses have large tails on the RHS of the peaks, respectively. The off-center penetration can run through more than four crystals (see the right peak in the figure).

The response function of Fig. 3 can be obtained by tracing a primary photon at a radial position through the surface center of the first encountered crystal until the last encountered crystal. The probability of being detected by a given crystal is the average over the width of the first encountered crystal's surface. The values used to compute the average associated with the given crystal are shown in Fig. 2.

The modified detector response has an advantage in modeling the measurements from individual crystals, since the response function is directly related to those individual crystals which are associated with the penetration of each primary photon. The modified response function can be used to restore the off-center resolution that is deteriorated by crystal penetration. Since the modified detector response is simulated for the primary photons impacting on the whole area of the front face of each crystal (at normal angle for the central crystal and oblique angles for the off-center crystals, see the right of Fig. 1), the nonuniform sampling effect will also be considered in the restoration. The restoration is performed from the sinogram to the projections with a uniform sampling size across the FOV at each projection angle.

The restoration procedures are depicted by Fig. 4. Let $\mathbf{Y}(\theta)$ be the data vector of a parallel-ray projection at projection angle θ (see the left of Fig. 4), which is selected from the sinogram of the ring detector. There are 600 such nonuniform sampled projections. Each vector $\mathbf{Y}(\theta)$ has either 100 or 101 elements, depending on the projection angle. The central element does not experience the crystal penetration, but the other elements do. The central crystal has the sampling size of $a/2 = 1.57$ mm, and others have smaller sampling size,

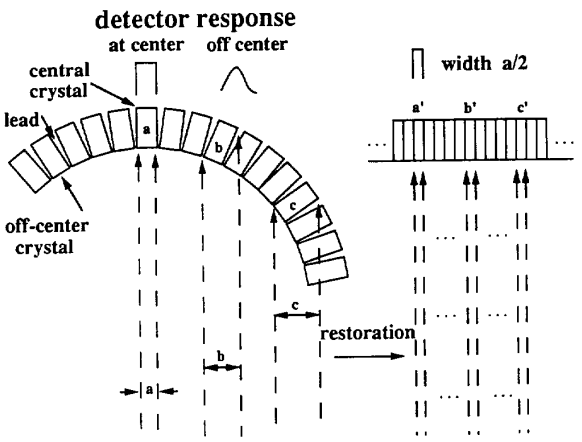

Fig. 4. The restoration from the sinogram sampled from the ring detector to the projections "acquired" by a perfect flat detector at different projection angles. Since a PET has a sampling size equal to approximately half of the crystal size, the restored projections have a uniform sampling size of $a/2$.

because the projecting sizes of the off-center crystal's front surfaces on the FOV are smaller (see the right of Fig. 1). Let $\mathbf{X}(\theta)$ be the restored data vector from the measured vector $\mathbf{Y}(\theta)$. The restored vector can be assumed as "acquired" by a "perfect" linear array of detectors at projection angle θ (see the right of Fig. 4.). The restored vector $\mathbf{X}(\theta)$ has 192 elements and a uniform sampling size of $a/2 = 1.57$ mm. The relation between the restored uniformly sampled projection $\mathbf{X}(\theta)$ and the measured projection $\mathbf{Y}(\theta)$ of the sinogram from the ring detector system is:

$$Y_i(\theta) = \Sigma_{j=1}^{J} R_{ij} X_j(\theta) + N_i(\theta), \quad i = 1, 2, \ldots, I \qquad (3)$$

where R_{ij} represents the detector response of Fig. 3, N_i is the Poisson noise associated with the mean $\Sigma_j R_{ij} X_j$, and I and J are the dimensions of vectors $\mathbf{Y}(\theta)$ and $\mathbf{X}(\theta)$, respectively. It is noted that the coincident response of pair-photon detection (which has, for very high stopping-power detector crystals, a rectangular form near either detector and a triangle form at the center of the detector pair) is neglected in (3). The distance-dependent effect of coincident response can be accurately compensated during image reconstruction [25], but not in the restoration of Fig. 4. If the noise level is very low, the restoration could be accomplished by inverting (3):

$$\mathbf{X}(\theta) = R^{-1}\mathbf{Y}(\theta). \qquad (4)$$

In practical situations, the noise level is relatively high, the inversion of (4) will boost the noise level in the restored projections $\mathbf{X}(\theta)$ [15], due to the underdetermined and ill-posed nature of (4) [26].

By modeling the data noise N_i as Poisson distributed around the mean $\Sigma_j R_{ij} X_j$, and assuming that the noise is spatially uncorrelated, a penalized maximum-likelihood (ML) algorithm can be derived as [27]:

$$\mathbf{X}_k^{(n+1)} = \overline{X}_k^{(n)} \frac{\Sigma_i R_{ik}[Y_i / \Sigma_j R_{ij} X_j^{(n)}]}{\Sigma_i R_{ik}}. \qquad (5)$$

The algorithm performs the restoration iteratively for each projection angle θ, where $\overline{X}_k$ is the smoothed value of X_k using, for example, a Gaussian filter with a full-width-at-half-maximum (FWHM) of three projection-bin units (or $3a/2$ mm).

After the restoration is accomplished by (5), the projections $\mathbf{X}(\theta)$ are first Fourier transformed and filtered (by, e.g., a Ramp filter with cutoff at the Nyquist frequency) in frequency space, then inverse Fourier transformed back to projection space, and finally backprojected to reconstruct the image. This filtering/backprojecting process is identical to the conventional filtered backprojection (FBP) reconstruction [28]. It is noted that during the process of backprojecting $\mathbf{X}(\theta)$, the distance-dependent blurring effects of the positron range, the nonparallel flight of pair photons and the coincident response of pair-photon detection can be compensated in a similar manner as that of collimator divergence in single photon emission computed tomography [25], [29].

Since the corrections for attenuation and scatter can be achieved in projection space [30], [31], and because the size of the blurring kernel associated with the positron range, the nonparallel flight of pair photons and the coincidence response of pair-photon detection is small (as compared to the size of FOV), that approach, which performs the restoration in projection space and the deblurring in image space [during the process of backprojecting $\mathbf{X}(\theta)$], may be the most efficient way for the reconstruction of high resolution PET systems.

The restoration using (5) for the uniformly sampled projections and the reconstruction using FBP from the restored uniformly-sampled projections were tested by computer simulations. The computer programs for the restoration and reconstruction were coded in Fortran language. The program codes were executed on a HP/730 desktop computer. The results are reported below.

III. Results

A chest phantom with a few small circular "cold" objects ($\approx$4 mm diameter) located at the center and near the periphery of the FOV was computer generated as shown in Fig. 5. The profile was drawn through the phantom center horizontally. From the phantom, the sinogram of the ring detector was simulated. A recursive line-tracing technique [32] was employed to compute each ray-sum through the chest phantom. Three sinograms were simulated. The first one considered the nonuniform sampling only by assuming that the crystal attenuation coefficient was very large. This is the projection model described in [33]. Each ray-sum intersected the first encountered crystal at the front surface of that crystal. Since each ray-sum was computed using the sampling size $a/2$, and was also computed taking into account whether a ray-sum intersected at two crystal's front surfaces, then those ray-sums which intersected two crystal's front surfaces were weighted to the two crystals. The weights were proportional to the intersecting area. The second one considered both the crystal penetration and the nonuniform sampling. In this case, each ray-sum was either detected by the first encountered crystal, or attenuated and detected by the next encountered crystal,

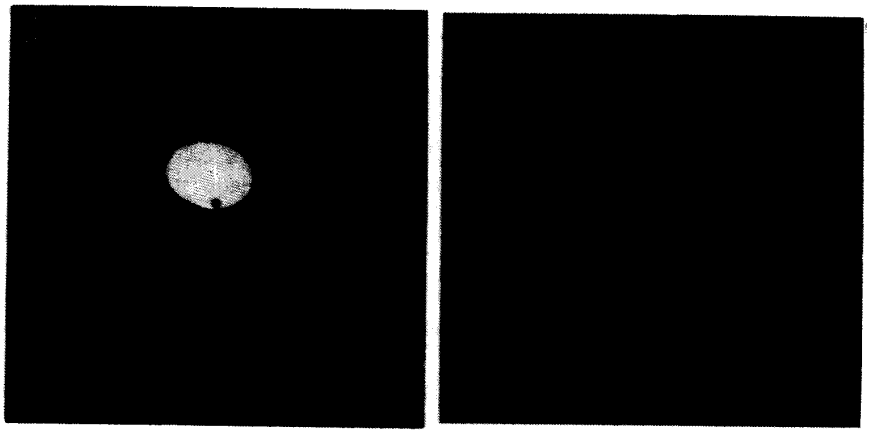

Fig. 5. The simulated mathematical phantom and the horizontal profile through the center.

or so on. The third sinogram was generated by imposing Poisson noise upon the second sinogram. The total counts were approximately one million.

Each sinogram $\{\mathbf{Y}(\theta)\}$ was first restored to produce the uniformly sampled "perfect" projections $\{\mathbf{X}(\theta)\}$ using algorithm of (5). Fig. 6 shows the iterative performance of that restoration algorithm for the sinograms. The test function is the root-mean-square error [28]:

$$\text{RMSE} = \sqrt{\Sigma_j (X_j^{(n)} - S_j)^2 / \Sigma_j (S_j - \overline{S})^2} \qquad (6)$$

where $\{S_j\}$ are the true ray-sums and $\overline{S}$ is the mean of $\{S_j\}$.

The solid curve labeled with noise-free was obtained from the second sinogram. The dotted curve labeled with unpenalized was obtained from the third (noisy) sinogram using the unpenalized ML algorithm [33] (i.e., ignoring the smoothing for $\overline{X}$ in (5)). The value after 20 iterations of this curve is expected to be smaller than that of the inversion method of (4), since the ML algorithm models the Poisson noise properties. The broken line shows the convergence performance of the penalized ML restoration algorithm of (5) for the noisy sinogram. This line goes up slightly in the first three iterations and then stays the same level for further iterations. In the following experiments, five iterations were chosen. A uniform initial estimate was used.

In order to show the impact of the projection-space restoration upon the reconstruction, the two-point interpolation method [34] was employed to map the sinogram to uniformly-sampled projections at all projection angles. And the reconstruction from the interpolated projections was compared to that from the restored projections. The interpolation does the mapping using the weights which are proportional to the intersecting areas of ray-sums with the crystal front surfaces. After interpolation, the same FBP reconstruction was applied to the interpolated projections, as that applied to the restored projections.

Fig. 7 shows the images reconstructed from the interpolated (top) and the restored (bottom) projections of the first sinogram. The profiles were drawn horizontally through the center of the images. The top reconstruction reflects the effect

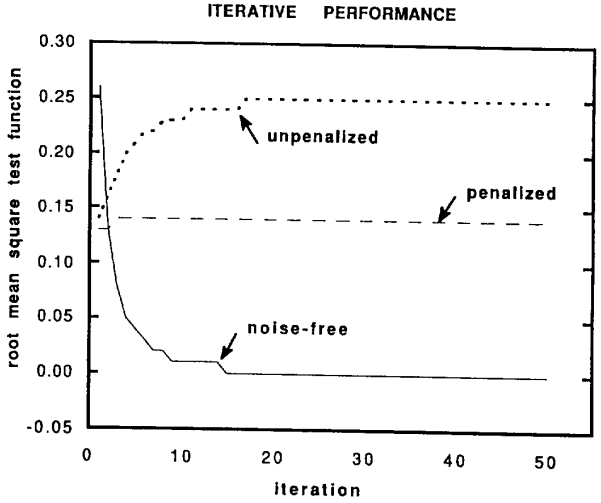

Fig. 6. The convergence performance of the iterative ML restoration algorithm for the noise-free and noisy sinograms. The test function is the root-mean-square error.

of nonuniform sampling. The off-center resolution is slightly better than the central resolution. This result is expected because of smaller sampling size. But the off-center image intensity is lower than that at the center because of the smaller sampling size. The radial fall off of intensity is accentuated near FOV periphery, due to the rapid change of sampling size there. It is clear that a conventional interpolation is not adequate for the nonuniform sampling across the FOV. The effect was compensated in the bottom image by restoration using the kernel R_{ij} with the assumption that μ_b was very large.

Fig. 8 shows the reconstructions from the interpolated (top) and the restored (bottom) projections of the second sinogram. The top image contains the effects of crystal penetration and nonuniform sampling. The image intensity near the FOV periphery is further lowered, as compared with that of Fig. 7. And the off-center resolution is degraded significantly, as

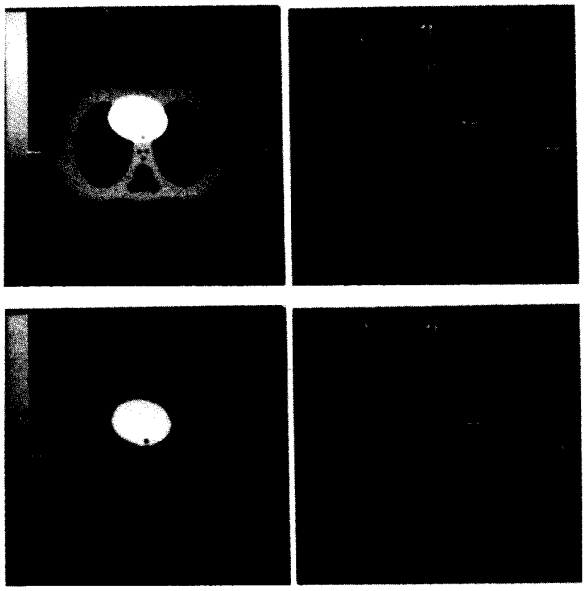

Fig. 7. The reconstructions from noise-free data considering the nonuniform sampling effect only with interpolation (top) and restoration (bottom). The horizontal profiles were drawn through the image centers. The restoration was iterated five times. The reconstruction was performed by FBP.

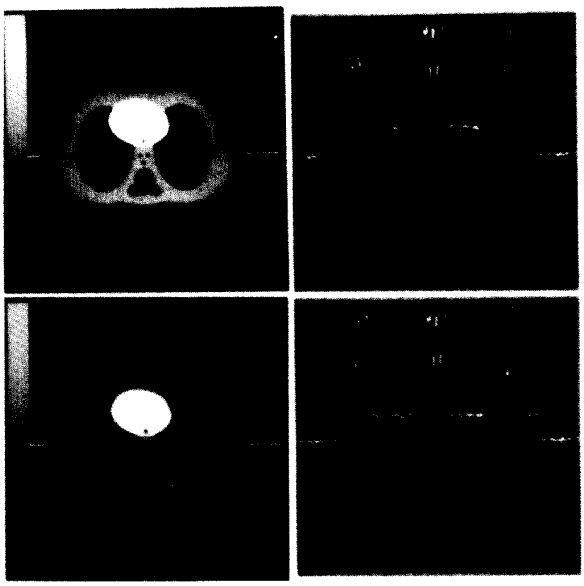

Fig. 8. The reconstructions from noise-free data considering both the crystal penetration and nonuniform sampling effects with interpolation (top) and restoration (bottom). The horizontal profiles ran through the image centers. The restoration was iterated 5 times. The reconstruction was performed by FBP.

compared with the central resolution. The bottom image demonstrates the success of the restoration by compensating for the effects with the kernel of Fig. 3.

The results obtained using the noisy sinogram are shown by Fig. 9. The top image was reconstructed from the interpolated projections of the sinogram, and the bottom one from the

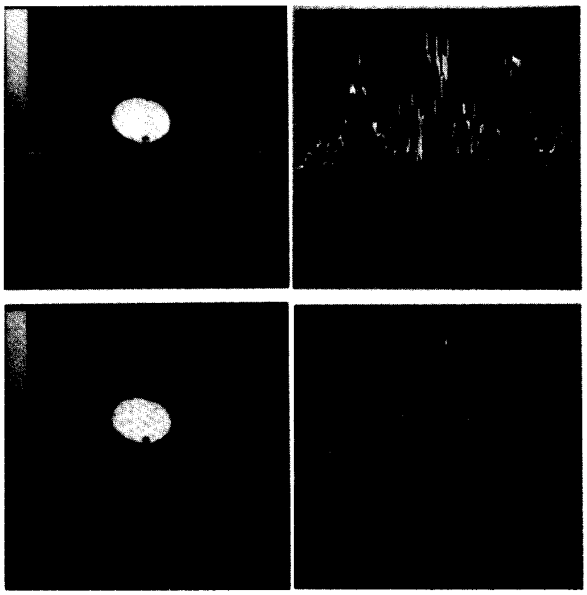

Fig. 9. The reconstructions from the noisy data considering the effects of crystal penetration and nonuniform sampling with interpolation (top) and restoration (bottom). The horizontal profiles ran through the image centers. The restoration was iterated five times. The reconstruction was performed by FBP.

restored projections. The off-center resolution of the reconstructions is clearly improved by the restoration, while the central resolution is preserved.

The restoration finished in less than one minute on the HP/730 workstation for five iterations, and the FBP reconstruction took approximately 3 minutes.

For comparison purpose, the crystal penetration and the nonuniform sampling were modeled in the projector/backprojector and were compensated in reconstructing the sinogram directly by the use of the unpenalized ML-EM algorithm [33]. Fig. 10 shows the reconstructions from the second (noise-free) sinogram after 500 iterations (on the top) and the third (noisy) sinogram after 100 iterations (on the bottom), respectively. The directly reconstructed images have a similar restored resolution, as compared to the images reconstructed from the restored projections using the FBP method. However, the direct reconstruction took 100 times more computation effort, as compared with the restoration/backprojection reconstruction. The heavy computational burden can be seen in the projection process, in which the uniform sampled ray-sums are first traced through the image array for each projection angle and then the detector response of Fig. 3 is applied to the ray-sums [see (5)] to generate the sinogram. The projection and backprojection need be repeated more than 100 times (or 100 iterations) to obtain the satisfactory result, as shown in the example of Fig. 10.

IV. Discussion

The described restoration for the detector response has the following features: (1) it is efficient in computation; (2) it is

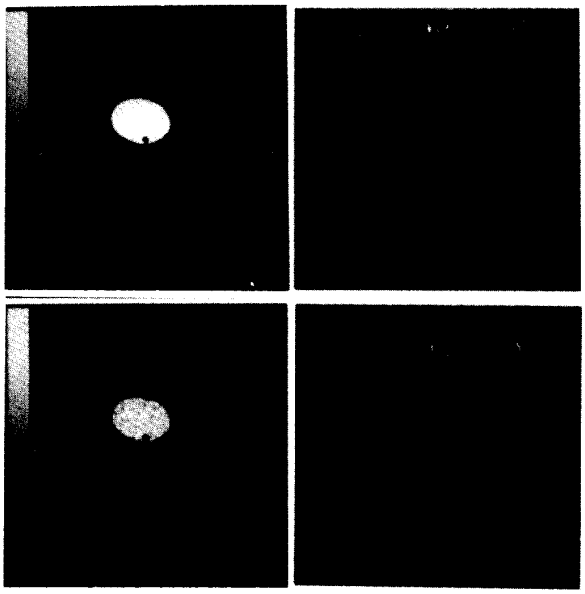

Fig. 10. The ML-EM reconstructions from the noise-free data after 500 iterations (top) and the noisy data after 100 iterations (bottom). The compensation for the effects of crystal penetration and nonuniform sampling was performed directly during reconstruction. The horizontal profiles were drawn through the image centers.

effective for resolution recovery; and (3) it is robustious in noise suppression.

The restoration/backprojection method may be extended to include (1) the correction for attenuation and scatter in projection space [30], [31] and (2) the compensation for the distance-dependent blurring of positron range, nonparallel flight of pair photons and coincident response of pair-photon detection in image space during backprojecting the restored projections [2], [3], [12].

The attenuation can be corrected by dividing the restored projections with the corresponding attenuation factors [30]. For the scatter correction [31], one has to be cautious since the correction in projection space may change the effects of nonuniform attenuator, activity out of FOV, etc.

The blurring of positron range and nonparallel flight of pair photons can be described by a Gaussian function with FWHM dependent on the distance from the center of the detector pair. The coincident response of pair-photon detection can be modeled as a convolution of two response functions: one is the detector response described above, and the other is the ideal coincident response which is rectangular near either detector and triangular at the center of the detector pair. The total blurring due to the distance-dependent effects is then modeled by the convolution of the Gaussian function and the coincident response. Once the blur kernel is formulated, the compensation can be carried out by the distance-dependent convolution as described in [25], [29].

The major limitation of this restoration/backprojection approach can be expressed as that the coherent physical characteristics of pair-photon detection is treated separately. The treatment may introduce errors. The comparison between measured sinograms and modeled projections using the method described above will show the accuracy of this approach, and so is necessary in the future research.

V. Conclusion

A mathematical approach to model the detector response due to crystal penetration and/or nonuniform sampling of a close-packed small-crystal ring PET system was studied. The restoration from the sinogram of the ring detector system to the uniformly-sampled "perfect" projections was tested by computer simulations. The reconstructions showed significant improvement in the off-center resolution, while preserving the central resolution across the FOV. Noise propagation in the restoration was suppressed.

With more powerful computers available, the method of directly reconstructing the sinogram will be more beneficial by improving the quantification of the reconstructions. Furthermore, the physical aspects of the positron annihilation, pair-photon detection, photon attenuation, and noise characteristics can be more accurately modeled in the method.

Acknowledgment

The author appreciates Dr. T. Turkington for providing the display program and Dr. Gene Gindi for preparing the manuscript.

References

[1] T. F. Budinger, S. E. Derenzo, and G. T. Gullberg, et al., "Emission computer assisted tomography with single-photon and positron annihilation photon emitters," *JCAT*, vol. 1, pp. 131–145, 1977.

[2] M. E. Phelps, "Emission computed tomography," *Seminars in Nucl. Med.*, vol. 7, pp. 337–365, 1977.

[3] G. Muehllehner and J. S. Karp, "Positron emission tomography imaging—technical considerations," *Seminars in Nucl. Med.*, vol. 14, pp. 35–50, 1986.

[4] E. Tanaka, "Recent progress on single photon and positron emission tomography—from detectors to algorithms," *IEEE Trans. Nucl. Sci.*, vol. 34, pp. 313–320, 1987.

[5] T. Tomitani, N. Nohara, and H. Morayama, et al., "Development of a high resolution PET for animal studies," *IEEE Trans. Nucl. Sci.*, vol. 32, pp. 822–825, 1985.

[6] A. Ricci, E. Hoffman, and M. Phelps, et al., "Investigation of a technique for providing a pseudo-continuous detector ring for positron tomography," *IEEE Trans. Nucl. Sci.*, vol. 29, pp. 452–456, 1982.

[7] G. Muehllehner and J. S. Karp, "A position camera using positron-sensitive detectors: PENN-PET," *J. Nucl. Med.*, vol. 27, pp. 90–98, 1986.

[8] H. B. Min, J. B. Ba, and K. J. Jung, et al., "Detector identification in a 4×4 BGO crystal array coupled to two dual PMTs for high resolution PET," *IEEE Trans. Nucl. Sci.*, vol. 34, pp. 332–336, 1987.

[9] C. Carrier, C. Martel, and D. Schmitt, et al., "Design of a high resolution PET using solid state scintilation detectors," *IEEE Trans. Nucl. Sci.*, vol. 35 pp. 685–690, 1988.

[10] S. E. Derenzo, T. F. Budinger, and T. Vuletich, "High resolution PET using narrow BGO crystals and individual photosensors," *IEEE Trans. Nucl. Sci.*, vol. 30, pp. 665–670, 1983.

[11] J. A. McIntyre, R. L. Spross, and K. H. Wang, "Construction of a PET with 2.4 mm detectors," *IEEE Trans. Nucl. Sci.*, vol. 33, pp. 425–427, 1986.

[12] S. E. Derenzo, "Mathematical removal of positron range blurring in high resolution tomography," *IEEE Trans. Nucl. Sci.*, vol. 33, pp. 565–569, 1986.

[13] J. S. Karp and M. E. Daube-Witherspoon, "Determination of depth-of-interaction in scintillation crystals using a temperature gradient," *Nucl. Instr. Meth.*, vol. A260, pp. 509–517, 1987.

[14] S. E. Derenzo, W. W. Moses, and H. G. Jackson, et al., "Initial characterization of a position-sensitive photodiode/BGO detection for PET," *IEEE Trans. Nucl. Sci.*, vol. 36, pp. 1084–1089, 1989.
[15] R. H. Huesman, E. M. Salmeron, and J. R. Baker, "Compensation for crystal penetration in high resolution positron tomography," *IEEE Trans. Nucl. Sci.*, vol. 36, pp. 1100–1107, 1989.
[16] W. H. Wong, "Designing a stratified detection system for PET cameras," *IEEE Trans. Nucl. Sci.*, vol. 33, pp. 591–596, 1986.
[17] C. J. Thompson, "The effects of detector material and structure on PET spatial resolution and efficiency," *TEEE Trans. Nucl. Sci.*, vol. 37, pp. 719–724, 1990.
[18] P. Bartzakos and C. J. Thompson, "A PET detector with depth-of-interaction determination," *Phys. Med. Biol.*, vol. 36, pp. 735–748, 1991.
[19] S. E. Derenzo, R. H. Huesman, and J. L. Cahoon, et al., "Initial results from the Donner 600 crystal positron tomography," *IEEE Trans. Nucl. Sci.*, vol. 34, pp. 321–325, 1987.
[20] S. E. Derenzo, R. H. Huesman, and J. L. Cahoon, et al., "A positron tomograph with 600 BGO crystals and 2.6 mm resolution," *IEEE Trans. Nucl. Sci.*, vol. 35, pp. 659–664, 1988.
[21] R. Lecomte, D. Schmitt, and G. Lamoureux, "Geometry study of a high resolution PET detector system using small detectors," *IEEE Trans. Nucl. Sci.*, vol. 31, pp. 556–561, 1984.
[22] T. J. Holmes and D. C. Ficke, "Analysis of positron-emission tomography scintillation detectors with wedge faces and inter crystal septa," *IEEE Trans. Nucl. Sci.*, vol. 32, pp. 826–830, 1985.
[23] N. A. Keller and L. R. Lupton, "PET detector ring aperture function calculations using Monte Carlo techniques," *IEEE Trans. Nucl. Sci.*, vol. 30, pp. 676–680, 1983.
[24] S. Schmitt, B. Karuta, and C. Carrier et al., "Fast point spread function computation from aperture functions in high-resolution PET," *IEEE Trans. Med. Imaging*, vol. 7, pp. 2–12, 1988.
[25] Z. Liang, "A 3D model for simultaneous compensation for non-uniform attenuation and collimator divergence in SPECT image reconstruction," *J. Nucl. Med.*, vol. 32, pp. 917, 1991.
[26] A. Tikhonov, V. Arsenin, and F. John, *Solutions of Ill-Posed Problems*. New York: Wiley, 1977.
[27] Z. Liang, "Implementation of non-linear filters for iterative penalized ML image reconstruction," *Conf. Record NSS-MIC*, vol. 2, pp. 1518–1522, 1990.
[28] R. H. Huesman, G. T. Gullberg, and W. Greenberg, et al., *User Manual: Donner Algorithm for Reconstruction Tomography*. Lawrence Berkeley Laboratory, 1977.
[29] Z. Liang, "Compensation for attenuation, scatter, and detector response in SPECT reconstruction via iterative FBP methods," *Med. Physics*. vol. 20, pp. 1097–1106, 1993.
[30] S. C. Huang, E. J. Hoffman, and M. E. Phelps, et al., "Quantitation in PET: 2. Effects of inaccurate attenuation correction," *JCAT*, vol. 3, pp. 804–814, 1979.
[31] M. Bergstrom, L. Eriksson, and C. Bohm, et al., "Correction for scattered radiation in a ring detector positron camera by integral transformation of the projections," *JCAT*, vol. 7, pp. 42–50, 1983.
[32] R. Sidon, "Fast calculation of the exact radiological path for a 3D CT array," *Med. Physics*, vol. 12, pp. 252–255, 1985.
[33] L. Shepp and Y. Vardi, "Maximum likelihood reconstruction for emission tomography," *IEEE Trans. Med. Imaging*, vol. 1, pp. 113–122, 1982.
[34] T. Peters, "Algorithms for fast back-and-reprojection in CT," *IEEE Trans. Nucl. Sci.*, vol. 28, pp. 3641–3647, 1981.